Asymmetric intraseasonal events in the stochastic skeleton MJO model with seasonal cycle

Sulian Thual [(1)], Andrew J. Majda [(1)], and Samuel N. Stechmann [(2)]

(1) Department of Mathematics, and Center for Atmosphere Ocean Science, Courant Institute of Mathematical Sciences, New York University, 251 Mercer Street, New York, NY 10012 USA

(2) Department of Mathematics, and Department of Atmospheric and Oceanic Sciences, University of Wisconsin - Madison, 480 Lincoln Drive, Madison, WI 53706 USA

Corresponding author:

Sulian Thual, 251 Mercer Street, New York, NY 10012 USA, *sulian.thual@gmail.com*

Revised for Climate Dynamics, June 2014

Abstract

The stochastic skeleton model is a simplified model for the Madden-Julian oscillation (MJO) and intraseasonal-planetary variability in general involving coupling of planetary-scale dry dynamics, moisture, and a stochastic parametrization for the unresolved details of synoptic-scale activity. The model captures the fundamental features of the MJO such as the intermittent growth and demise of MJO wave trains, the MJO propagation speed, peculiar dispersion relation, quadrupole vortex structure, etc. We analyze here the solutions of a stochastic skeleton model with an idealized seasonal cycle, namely a background warm pool state of heating/moistening displacing meridionally during the year. The present model considers both equatorial and off-equatorial components of the envelope of synoptic scale convective activity, which allows for a large diversity of meridionally symmetric and asymmetric intraseasonal events found in nature. These include examples of symmetric events with MJO quadrupole vortex structure, half-quadrupole events with off-equatorial convective heating structure, as well as tilted events with convective heating structure oriented north-westward and associated northward propagation that is reminiscent of the summer monsoon intraseasonal oscillation. The model also reproduces qualitatively the meridional migration of intraseasonal variability during the year, that approximatively follows the meridional migration of the background warm pool.

1 Introduction

The dominant component of intraseasonal variability in the tropics is the 40 to 50 day intraseasonal oscillation, often called the Madden-Julian oscillation (MJO) after its discoverers (Madden and Julian, 1971; 1994). In the troposphere, the MJO is an equatorial planetary-scale wave, that is most active over the Indian and western Pacific Oceans and propagates eastward at a speed of around $5\,ms^{-1}$. The planetary-scale circulation anomalies associated with the MJO significantly affect monsoon development, intraseasonal predictability in midlatitudes, and the development of El Niño events in the Pacific Ocean, which is one of the most important components of seasonal prediction.

One fundamental and not fully understood characteristic of the MJO and the intraseasonal oscillation (ISO) in the tropics in general is its pronounced seasonality. The MJO signals migrate in latitude during the year, approximatively following the migration of warm sea surface temperatures, with for example a peak activity of zonal winds and precipitation located slightly south of the equator in boreal winter and north of the equator in boreal summer (Salby and Hendon, 1994; Zhang and Dong, 2004). The MJO is strongest during the boreal winter and spring seasons where it appears as a predominantly eastward propagating system of convection along (or sligthly south of) the equator. Noteworthy the MJO signals in boreal winter are related to the onset and breaks of the Australian monsoon (Wheeler and Hendon, 2004; Lau and Waliser, 2012 chapt 5).

In boreal summer, the ISO is of a different character: the dominant intraseasonal oscillation, of period 30-60 days, shows a pronounced off-equatorial component that is associated in particular with northward or north-eastward propagation of convection over the Indian Ocean and the Asian continent (Zhang, 2005; Kikuchi et al., 2011). This intraseasonal mode is sometimes referred to as the summer monsoon ISO, or boreal summer ISO, in order to differentiate it from the boreal winter MJO. Several studies interpret the northward propagation as resulting from the interaction between the eastward propagation of convection at the equator (e.g. the northern gyre of equatorial Rossby waves forced by equatorial convective heating) and the background mean state (Lau and Peng, 1990; Wang and Xie, 1997; Lawrence and Webster, 2002), though there is also observational and theoretical evidence that northward propagation can be independent (Webster, 1983; Wang and Rui, 1990; Jiang et al., 2004; Annamalai and Sperber, 2005). The summer monsoon ISO signals are strongly related to the onset and breaks of the South Asian and East Asian monsoon (Lau and Waliser, 2012 chapt 2, 3).

In addition to such climatological features, the structure of individual intraseasonal events is often unique. For example, both equatorial and off-equatorial convective heating coexist during intraseasonal events with characteristics and intensity that differ from one event to another (Wang and Rui, 1990; Jones et al., 2004; Masunaga, 2007), including during MJO events (Tung et al., 2014a, b). Biello and Majda (2005, 2006) for example have analyzed in a multiscale model for the MJO the differences in planetary-scale circulation induced by equatorial or off-equatorial convective heating of synoptic-scale. Individual intraseasonal events also show unique refined vertical structures as well as complex dynamic and convective features within their envelope. The MJO for example shows front-to-rear vertical tilts, westerly wind bursts, etc within its envelope (Kikuchi and Takayabu, 2004; Kiladis et al., 2005; Tian et al., 2006), while the summer monsoon ISO shows dynamic and convective features of a different nature (Goswami et al., 2003; Straub and Kiladis, 2003)

Despite the primary importance of the MJO and the decades of research progress since its original discovery, no theory for the MJO has yet been generally accepted. Simple theories provide some useful insight on certain isolated aspects of the MJO, but they have been largely unsuccessful in reproducing all of its fundamental features together (Zhang, 2005). Meanwhile, present-day simulations by general circulation models (GCMs) typically have poor representations of it, despite some recent improvements (Lin et al., 2006; Kim et al., 2009; Hung et al., 2013). A growing body of evidence suggests that this poor performance of both theories and simulations in general is due to the inadequate treatment of the organized structures of tropical convection (convectively-coupled waves, cloud-clusters...), that are defined on a vast range of spatiotemporal scales (synoptic, mesoscale...) and that generate the MJO as their planetary envelope (Hendon and Liebmann, 1994; Moncrieff et al., 2007). For example, in current GCMs and models in general computing resources significantly limit spatial grids (to $\approx 10 - 100\,km$), and therefore there are several important small scale moist processes that are unresolved or parametrized according to various recipes. Insight has been gained from the study of MJO-like waves in multicloud model simulations and in superparametrization computer simulations, which appear to capture many of the observed features of the MJO by accounting for coherent smaller-scale convective structures within the MJO envelope (e.g. Grabowski and Moncrieff, 2004; Majda et al., 2007; Khouider et al., 2011; Ajayamohan et al., 2013). Suitable stochastic parametrizations also appear to be good canditates to account for irregular and intermittent organized small scale moist processes while remaining computationally efficient (Majda et al., 2008; Khouider et al., 2010; Stechmann and Neelin, 2011; Frenkel et al., 2012; Deng et al., 2014). As another example, the role of synoptic scale waves in producing key features of the MJO's planetary scale envelope has been elucidated in multiscale asymptotic models (Majda and Biello, 2004; Biello and Majda, 2005, 2006; Majda and Stechmann, 2009a; Stechmann et al., 2013).

While theory and simulation of the MJO remain difficult challenges, they are guided by some generally accepted, fundamental features of the MJO on intraseasonal-planetary scales that have been identified relatively clearly in observations (Hendon and Salby, 1994; Wheeler and Kiladis, 1999; Zhang, 2005). These features are referred to here as the MJO's "skeleton" features:

I. A slow eastward phase speed of roughly $5\,ms^{-1}$,

II. A peculiar dispersion relation with $d\omega/dk \approx 0$,

III. A horizontal quadrupole structure,

IV. Intermittent generation of MJO events,

V. Organization of MJO events into wave trains with growth and demise.

Recently, Majda and Stechmann (2009b) introduced a minimal dynamical model, the skeleton model, that captures the MJO's intraseasonal features (I-III) together for the first time in a simple model. The model is a coupled nonlinear oscillator model for the MJO skeleton features as well as tropical intraseasonal variability in general. In particular, there is no instability mechanism at planetary scale, and the interaction with sub-planetary convective processes discussed above is accounted for, at least in a crude fashion. In a collection of numerical experiments, the nonlinear skeleton model has been shown to simulate realistic MJO events with significant variations in occurrence and strength, asymmetric east-west structures, as well as a preferred localization over the background state warm pool region (Majda and Stechmann, 2011). More recently, a stochastic version of the skeleton model has been developed that reproduces qualitatively features (IV-V) (Thual et al., 2014). The stochastic skeleton model reproduces the intermittent growth and demise of MJO wave trains found in nature, or in other words the occurence of series of successive MJO events, either two, three or sometimes more in a row (Matthews, 2008; Yoneyama et al., 2013). In the stochastic skeleton model, a simple stochastic parametrization allows for an intermittent evolution of the unresolved synoptic-scale convective/wave processes and their planetary envelope. This stochastic parametrization follows a similar strategy found in the related studies mentioned above (e.g. as reviewed in Majda et al., 2008).

In the present article, we will examine the solutions of a stochastic skeleton model with seasonal cycle. While previous work on the skeleton model has focused essentially on the MJO, we focus here on the tropical intraseasonal variability in general, as discussed above. Two main features of the intraseasonal variability that are qualitatively reproduced by the model are:

VI. Meridionally asymmetric intraseasonal events, and

VII. A seasonal modulation of intraseasonal variability.

Indeed, we will show that the stochastic skeleton model with seasonal cycle reproduces a large diversity of intraseasonal events found in nature, with for example some characteristics reminiscent of both the MJO and the summer monsoon ISO. This occurs despite the fact that important details such as land-sea contrast, shear, tilted vertical structure, and continental topography are not treated in the model. In addition, we will show that the model reproduces qualitatively the meridional migration of the intraseasonal variability during the year. In order to account for features (VI-VII), two important modifications are considered in the stochastic skeleton model with seasonal cycle. First, while in previous works with the skeleton model focusing on the MJO (Majda and Stechmann, 2009b, 2011; Thual et al., 2014) a single equatorial component of convective heating was considered, here we consider additional off-equatorial components of convective heating in order to further produce meridionally asymmetric intraseasonal events beyond the MJO. Second, a simple seasonal cycle is included that consists of a background warm pool state of heating/moistening that migrates meridionally during the year.

The article is organized as follows. In section 2 we recall the design and main features of the skeleton model, and present the stochastic skeleton model with seasonal cycle used here. In section 3 we present the main features of the model solutions, including their zonal wavenumber-frequency power spectra and seasonal modulation, as well as several hovmoller diagrams. In section 4 we focus on three interesting types of intraseasonal events found in the model solutions and analyze their potential observational surrogates, their approximate structure and occurence through the year. Section 5 is a discussion with concluding remarks.

2 Model Formulation

2.1 Stochastic Skeleton Model

The skeleton model has been proposed originally by Majda and Stechmann (2009b) (hereafter MS2009), and further analyzed in Majda and Stechmann (2011) (hereafter MS2011) and Thual et al. (2014) (hereafter TMS2014). It is a minimal non-linear oscillator model for the MJO and the intraseasonal-planetary variability in general. The design of the skeleton model, already presented in those previous publications, is recalled here for completeness.

The fundamental assumption in the skeleton model is that the MJO involves a simple multiscale interaction between (i) planetary-scale dry dynamics, (ii) lower-level moisture q and (iii) the planetary-scale envelope of synoptic-scale convection/wave activity, a. The planetary envelope a in particular is a collective (i.e. integrated) representation of the convection/wave activity occurring at sub-planetary scale (i.e. at synoptic-scale and possibly at mesoscale), the details of which are unresolved. A key part of the $q-a$ interaction is how moisture anomalies influence convection. Rather than a functional relationship $a=a(q)$, it is assumed that q influences the tendency (i.e. the growth and decay rates) of the envelope of synoptic activity:

$$\partial_t a = \Gamma q a\,, \tag{1}$$

where $\Gamma > 0$ is a constant of proportionality: positive (negative) low-level moisture anomalies create a tendency to enhance (decrease) the envelope of synoptic activity.

The basis for Eq. (1) comes from a combination of observations, modeling, and theory. Generally speaking, lower-tropospheric moisture is well-known to play a key role in regulating convection (Grabowski and Moncrieff, 2004; Moncrieff, 2004; Holloway and Neelin, 2009), and has been shown to lead the MJO's heating anomalies (Kikuchi and Takayabu, 2004; Kiladis et al., 2005; Tian et al., 2006), which suggests the relationship in Eq. (1). This relationship is further suggested by simplified models for synoptic-scale convectively coupled waves showing that the growth rates of the convectively coupled waves depend on the wave's environment, such as the environmental moisture content (Khouider and Majda, 2006; Majda and Stechmann, 2009a; Stechmann et al., 2013). In particular, Stechmann et al. (2013) estimate the value of Γ from these growth rate variations.

In the skeleton model, the $q-a$ interaction parametrized in Eq. (1) is further combined with the linear primitive equations projected on the first vertical baroclinic mode. This reads, in non-dimensional units,

$$\begin{aligned}
&\partial_t u - yv - \partial_x \theta = 0\\
&yu - \partial_y \theta = 0\\
&\partial_t \theta - (\partial_x u + \partial_y v) = \overline{H}a - s^\theta\\
&\partial_t q + \overline{Q}(\partial_x u + \partial_y v) = -\overline{H}a + s^q
\end{aligned} \tag{2}$$

with periodic boundary conditions along the equatorial belt. The first three rows of Eq. (2) describe the dry atmosphere dynamics, with equatorial long-wave scaling as allowed at planetary scale. The u and v are the zonal and meridional velocity, respectively, θ is the potential temperature and in addition $p = -\theta$ is the pressure. The fourth row describes the evolution of low-level moisture q. All variables are anomalies from a radiative-convective equilibrium, except a. In order to reconstruct the complete fields having the structure of the first vertical baroclinic mode, one must use $u(x, y, z, t) = u(x, y, t)\sqrt{2}cos(z)$, $\theta(x, y, z, t) = \theta(x, y, t)\sqrt{2}sin(z)$, etc., with a slight abuse of notation. This model contains a minimal number of parameters: $\overline{Q}$ is the background vertical moisture gradient, Γ is a proportionality constant. The $\overline{H}$ is irrelevant to the dynamics (as can be seen by rescaling a) but allows us to define a heating/drying rate $\overline{H}a$ for the system in dimensional units. The s^{θ} and s^{q} are external sources of cooling and moistening, respectively, that need to be prescribed in the system (see hereafter). The skeleton model depicts the MJO as a neutrally-stable planetary wave. In particular, the linear solutions of the system of equations (1-2) (when a is truncated at the first Hermite function component, see hereafter) exhibit a MJO mode with essential observed features, namely a slow eastward phase speed of roughly $5\,ms^{-1}$, a peculiar dispersion relation with $d\omega/dk \approx 0$ and a horizontal quadrupole structure (MS2009; MS2011).

The stochastic skeleton model, introduced in TMS2014, is a modified version of the skeleton model from Eq. (1-2) with a simple stochastic parametrization of the synoptic scale processes. The amplitude equation (1) is replaced by a stochastic birth/death process (the simplest continuous-time Markov process) that allows for intermittent changes in the envelope of synoptic activity (see chapter 7 of Gardiner, 1994; Lawler, 2006). Let a be a random variable taking discrete values $a = \Delta a\, \eta$, where η is a positive integer. The probabilities of transiting from one state η to another over a time step Δt read as follows:

$$\begin{aligned}
&P\{\eta(t+\Delta t) = \eta(t)+1\} = \lambda \Delta t + o(\Delta t)\\
&P\{\eta(t+\Delta t) = \eta(t)-1\} = \mu \Delta t + o(\Delta t)\\
&P\{\eta(t+\Delta t) = \eta(t)\} = 1-(\lambda+\mu)\Delta t + o(\Delta t)\\
&P\{\eta(t+\Delta t) \neq \eta(t)-1,\, \eta(t),\, \eta(t)+1\} = o(\Delta t)\,,
\end{aligned} \tag{3}$$

where λ and μ are the upward and downward rates of transition, respectively. They read:

$$\lambda = \begin{cases} \Gamma |q| \eta + \delta_{\eta 0} \text{ if } q \geq 0 \\ \delta_{\eta 0} \text{ if } q < 0 \end{cases} \quad \text{and } \mu = \begin{cases} 0 \text{ if } q \geq 0 \\ \Gamma |q| \eta \text{ if } q < 0 \end{cases} \tag{4}$$

where $\delta_{\eta 0}$ is the kronecker delta operator. The above choice of the transition rates ensures that $\partial_t E(a) = \Gamma E(qa)$ for Δa small, where E denotes the statistical expected value, so that the $q - a$ interaction described in Eq. (1) is recovered on average.

This stochastic birth/death process allows us to account for the intermittent contribution of unresolved synoptic-scale details on the MJO. The synoptic-scale activity consists of a complex menagerie of convectively coupled equatorial waves, such as 2-day waves, convectively coupled Kelvin waves, etc (Kiladis et al., 2009). Some of these synoptic details are important to the MJO, as they can be both modulated by the planetary background state and contribute to it, for example through upscale convective momentum transport or enhanced surface heat fluxes (Majda and Biello, 2004; Biello and Majda, 2005, 2006; Moncrieff et al., 2007; Majda and Stechmann, 2009a; Stechmann et al., 2013). With respect to the planetary processes depicted in the skeleton model, the contribution of those synoptic details appears most particularly to be highly irregular, intermittent, and with a low predictability (e.g. Dias et al., 2013), which is parametrized by Eq. (3). This stochastic parametrization follows the same prototype found in previous related studies (Majda et al., 2008). The methodology consists in coupling some simple stochastic triggers to the otherwise deterministic processes, according to some probability laws motivated by physical intuition gained (elsewhere) from observations and detailed numerical simulations. Most notably, the stochastic skeleton model has been shown to reproduce qualitatively the intermittent growth and demise of MJO wave trains found in nature, i.e. the occurence of series of successive MJO events, either two, three or sometimes more in a row (Matthews, 2008; Yoneyama et al., 2013; TMS2014).

2.2 Meridionally Extended Skeleton Model

We now introduce a meridionally extended version of the stochastic skeleton model. Previous work on the skeleton model has focused essentially on the MJO dynamics, associated with an equatorial component of convective heating $\overline{H}a$ (MS2009, MS2011, TMS2014). In order to produce intraseasonal events beyond the MJO, with either a meridionally symmetric or asymmetric structure, we include here additional off-equatorial components of convective heating $\overline{H}a$ in the skeleton model. The meridionally extended skeleton model is efficiently solved using a pseudo-spectral method (i.e. using both spectral space and physical space) that is similar to the one from Majda and Khouider (2001), which is detailed below.

First, we consider a projection of the skeleton model variables from Eq. (2) on a spectral space consisting of the first M meridional Hermite functions $\phi_m(y)$ (see e.g. Biello and Majda, 2006):

$$a(x,y,t) = \sum_{m=0}^{M-1} A_m(x,t)\phi_m(y), \text{ with} \tag{5}$$

$$\phi_m(y) = \frac{H_m e^{-y^2/2}}{\sqrt{2^m m! \sqrt{\pi}}},\ 0 \le m \le M-1, \text{ and with Hermite polynomials } H_m(y) = (-1)^m e^{y^2} \frac{d^m}{dy^m} e^{-y^2} \tag{6}$$

This spectral space allows us to easily solve the dry dynamics component of the skeleton model (first three rows of Eq. 2). A suitable change of variables for this is to introduce K and R_m, $1 \le m \le M-2$, that are the amplitudes of the first equatorial Kelvin and Rossby waves, respectively. Their evolution reads:

$$\partial_t K + \partial_x K = -\frac{1}{\sqrt{2}} S_0 \tag{7}$$

$$\partial_t R_m - \frac{\partial_x R_m}{2m+1} = -\frac{2\sqrt{m(m+1)}}{2m+1}\left(\sqrt{m}S_{m+1} + \sqrt{m+1}S_{m-1}\right) \tag{8}$$

with $S_m = \overline{H}A_m - S_m^\theta$, $0 \le m \le M-1$. The variables from Eq. (2) can then be reconstructed as:

$$u(x,y,t) = \frac{K}{\sqrt{2}}\phi_0 + \sum_{m=1}^{M-2} \frac{R_m}{4}\left[\frac{\phi_{m+1}}{\sqrt{m+1}} - \frac{\phi_{m-1}}{\sqrt{m}}\right] \tag{9}$$

$$\theta(x,y,t) = -\frac{K}{\sqrt{2}}\phi_0 - \sum_{m=1}^{M-2} \frac{R_m}{4}\left[\frac{\phi_{m+1}}{\sqrt{m+1}} + \frac{\phi_{m-1}}{\sqrt{m}}\right] \tag{10}$$

$$v(x,y,t) = \frac{S_1}{\sqrt{2}}\phi_0 + \sum_{m=1}^{M-2}\left[\partial_x R_m + \sqrt{m+1}\,S_{m+1} - \sqrt{m}\,S_{m-1}\right]\frac{\phi_m}{\sqrt{2}(2m+1)} \tag{11}$$

Second, we consider a physical space consisting of an ensemble of M zonal "stochastic strips" with meridional positions y_l, $-(M-1)/2 \leq l \leq (M-1)/2$ given by the roots $\phi_M(y_l) = 0$ (with here M odd, though the method is also valid for M even). See Fig. 1 for the setup with $M = 5$. The values of the skeleton model variables on such stochastic strips reads:

$$a(x, y_l, t) = a_l(x,t) \tag{12}$$

One advantage of using these special points in physical space is that the spectral components A_m from Eq. (5) can be computed efficiently as:

$$A_m \approx \sum_{l=-(M-1)/2}^{(M-1)/2} a_l \phi_m(y_l)\overline{G}_l, \text{ with } \overline{G}_l = \frac{1}{M(\phi_{M-1}(y_l))^2}, \tag{13}$$

which follows from the Gauss-Hermite quadrature approximation (Majda and Khouider, 2001). This representation allows us to easily solve the moisture and stochastic component of the skeleton model (fourth row of Eq. 2 and Eq. 3). A suitable change of variables to achieve this is to introduce $Z = q + \overline{Q}\theta$, in order to solve for each zonal stochastic strip a local system of equations:

$$\partial_t Z_l = (\overline{Q} - 1)\overline{H} a_l + s_l^q - \overline{Q} s_l^\theta \tag{14}$$

as well as the stochastic process from Eq. (3) for each a_l (or η_l).

The spectral and physical space used in the present article are shown in Fig. 1. We consider here a meridional truncation $M = 5$ (i.e. 5 Hermites functions/zonal stochastic strips) that retains the main equatorial Kelvin and Rossby waves that are relevant for symmetric and asymmetric intraseasonal events (Gill, 1980; Biello and Majda 2005, 2006). This corresponds to one zonal stochastic strip at the equator and four strips off-equator. The spectral components of heating A_0, A_1, A_2 (with meridional profiles ϕ_0, ϕ_1, ϕ_2 shown in Fig. 1) may excite the equatorial Kelvin and first three Rossby waves from Eq. (7-8). Note that in previous work with the skeleton model for the MJO only (MS2009, MS2011, and TMS2014) a meridional truncation $M = 1$ was used, corresponding to a single zonal stochastic strip at the equator with associated component A_0 exciting the Kelvin and first Rossby symmetric waves.

2.3 Seasonal cycle warm pool

In the present article, we consider a background warm pool state of the meridionally extended skeleton model from section 2.2 that is seasonally varying. The background warm pool state migrates meridionally with seasons, in qualitative agreement with observations (Zhang and Dong, 2004). The sources of heating/moisture are balanced and read, in dimensional units ($K.day^{-1}$):

$$s^\theta = s^q = (1 - 0.6cos(2\pi x/L))\exp(-(y - y_C)^2/2), \text{ with} \tag{15}$$

$$y_C = Y\,sin(2\pi t/T) \tag{16}$$

where L is the equatorial belt length, T is the seasonal cycle period (one year), and $Y = 900\,km$. The background warm pool state in Eq. (15) consists of a maximal region of heating/moistening that extends from $x \approx 10,000 - 30,000$ km and that is centered around y_c, and a cold pool elsewhere. In boreal spring/autumn ($y_c = 0$) the background warm pool state is centered at the equator and its meridional profile matches the one of the Hermite function ϕ_0 shown in Fig. 1 (e.g. as in MS2011; TMS2014). The background warm pool displaces meridionally during the year, with its meridional center being $y_c = -Y$ in boreal winter, $y_C = 0$ in boreal spring/autumn, and $y_c = Y$ in boreal summer. This meridional displacement is qualitatively consistent with the one found in observations. However, here for simplicity the warm pool displacement is symmetric with respect to the equator; in nature the warm pool displacement is greater in boreal summer (around 1000 km north) than in boreal winter (around 600km south, see e.g. Fig. 4 of Zhang and Dong, 2004). As a result, a direct comparison of the model solutions with observations must be considered carefully.

The other reference parameters values used in this article are identical to TMS2014. They read, in non-dimensional units: $\overline{Q} = 0.9$, $\Gamma = 1.66$ ($\approx 0.3\, K^{-1} day^{-1}$), $\overline{H} = 0.22$ ($10\, K day^{-1}$), with stochastic transition parameter $\Delta a = 0.001$. Details on the numerical method used to compute the simulations can be found in appendix A of TMS2014. In the following sections of this article, simulation results are presented in dimensional units. The dimensional reference scales are x, y: 1500 km, t: 8 hours, u: $50\, m.s^{-1}$, θ, q: 15 K (see TMS2014).

3 Model Solutions

In this article we analyze the dynamics of the stochastic skeleton model with seasonal cycle in a statistically equilibrated regime. This section presents the main features of the model solutions, namely their zonal wavenumber-frequency power spectra, seasonal modulation, as well as several hovmoller diagrams.

3.1 Zonal wavenumber-frequency power spectra

The stochastic skeleton model with seasonal cycle simulates a MJO-like signal that is the dominant signal at intraseasonal-planetary scale, consistent with observations (Wheeler and Kiladis, 1999). Figure 2 shows the zonal wavenumber-frequency power spectra of model variables averaged within $1500km$ south/north as a function of the zonal wavenumber k (in $2\pi/40,000$ km) and frequency ω (in cpd). The MJO appears here as a power peak in the intraseasonal-planetary band ($1 \leq k \leq 3$ and $1/90 \leq \omega \leq 1/30$ cpd), most prominent in u, q and $\overline{H}a$. This power peak roughly corresponds to the slow eastward phase speed of $\omega/k \approx 5\, ms^{-1}$ with the peculiar relation dispersion $d\omega/dk \approx 0$ found in observations (Wheeler and Kiladis, 1999). Those results are consistent with the ones of TMS2014 (its Fig. 2 and 7), though the power spectra are here more blurred in comparison. We denote hereafter the band $1 \leq k \leq 3$ and $1/90 \leq \omega \leq 1/30$ cpd as the MJO band, which will be used to filter the model solutions in the next sections.

The other features in Fig. 2 are weaker power peaks near the dispersion curves of a moist Rossby mode (around $k \approx -2$ and $\omega \approx 1/90$ cpd) and of the dry uncoupled Kelvin and Rossby waves from Eq. (8) (see MS2009; TMS2014). We note that for an antisymmetric average ($0 - 1500km$

north minus $0 - 1500km$ south) the main feature is a power peak near the dispersion curve of the uncoupled Rossby wave R_2 (not shown).

3.2 Seasonal modulation

The intraseasonal variability in the stochastic skeleton model migrates meridionally during the year, approximatively following the meridional migration of the background warm pool. Figure 3 shows the seasonal variations of intraseasonal activity over the warm pool region, as a function of meridional position y. This diagnostic is somewhat similar to the one of Zhang and Dong (2004, Fig. 4). Figure 3(f) will be described in details in section 4.5.

This meridional migration of intraseasonal variability shares some similarities with the one observed in nature (Zhang and Dong, 2004), with overall an increased variability in the northern (southern) hemisphere in boreal summer (winter) as seen for all variables. The present model however considers a qualitative truncation of the planetary-scale circulation to a few main components (see section 2), and as result the meridional displacement of intraseasonal variability is strongly dependent on the meridional shape of the first equatorial Kelvin and Rossby waves. This displacement is different for each variable: the variable θ for example shows two strong off-equatorial components that approximatively match the off-equatorial gyres of the first symmetric Rossby wave structure (R_1) from Eq. (8-11). It is useful here to remember that $\theta = -p$ for the surface pressure p with our crude first baroclinic vertical truncation. The variables u and $\overline{H}a$ show strong equatorial components during the entire year that approximatively match the Kelvin wave structure (K), while the variables v and q show strong off-equatorial components that approximatively match the first antisymmetric Rossby wave structure (R_2).

3.3 $y - t$ Hovmoller diagrams

The stochastic skeleton model with seasonal cycle simulates a large diversity of intreaseasonal events, either meridionally symmetric or asymmetric, with a realistic intermittency. Figure 4(a-e) shows the $y - t$ Hovmollers diagrams of the model variables, filtered in the MJO band and considered in a meridional slice at the zonal center of the background warm pool ($x = 20,000\,km$).

Figure 4(f) shows the convective heating $\overline{H}a$ at different times in order to provide additional examples of intraseasonal events.

A new feature of the stochastic skeleton model with seasonal cycle as compared to previous work with the skeleton model (MS2009; MS2011; TMS2014) is the simulation of a large diversity of meridionally symmetric and asymmetric intraseasonal events, beyond the MJO. As seen in Fig. 4 on all model variables the intraseasonal events show a great diversity in meridional structure, localization, strength and lifetime. In Fig. 4(e-f), there are examples of intraseasonal events (hereafter symmetric events) with equatorial convective heating $\overline{H}a$ around time 72500 days, 75600 days, 76600 days, 79500 days, and of intraseasonal events (hereafter half-quadrupole events) with off-equatorial convective heating around time 74800 days, 77300 days, and 80100 days. Some intraseasonal events (hereafter tilted events) even exhibit apparent meridional propagations of convective heating, for example around time 73000 days, 73800 days, and 81700 days. The symmetric, half-quadrupole and tilted types of events are analyzed in further detail in the next section. In addition, the intraseasonal events in Fig. 4 are organized into intermittent wave trains with growth and demise, i.e. into series of successive intraseasonal events following a primary intraseasonal event, as seen in nature (Matthews, 2008; Yoneyama et al., 2013; TMS2014). This is an attractive feature of the stochastic skeleton model in generating intraseasonal variability.

4 Three types of intraseasonal events

Three interesting types of intraseasonal events are found in the solutions of the stochastic skeleton model with seasonal cycle: symmetric events, half-quadrupole events, and tilted events. In this section, we provide some carefully selected examples for each of those types of events and discuss their potential observational surrogates. We then analyze the approximate structures of the three types of event and their occurence in the model solutions.

4.1 Symmetric events

Figure 5 shows successive snapshots for an example of a symmetric intraseasonal event (for variables filtered in the MJO band). In Fig. 5, the symmetric event develops over the warm pool region $x \approx 10,000 - 30,000\,km$ and propagates eastward at a speed of around $5\,ms^{-1}$. The symmetric event consists of an equatorial center of convective heating $\overline{H}a$, with leading moisture anomalies q and a surrounding quadrupole vortex structure in θ and the relative vorticity denoted as $curl = \partial_x v - \partial_y u$.

The symmetric type of event is representative of MJO composites in nature (Hendon and Salby, 1994). It also has the structure of the MJO mode from MS2009. In Fig. 5, note in addition that the divergence matches the structure of $\overline{H}a$, consistent with the weak temperature gradient approximation being applied at large scales in the tropics (Sobel et al., 2001; Majda and Klein, 2003). This match is also found for the other types of intraseasonal events (see hereafter). Such approximation is relevant here to analyze a posteriori the simulation results, filtered in the MJO band, but is however not relevant in the full model dynamics (see the discussion in the appendix of MS2011). Note also that the curl has a main contribution from $-\partial_y u$ and very little contribution from $\partial_x v$, as expected from the long-wave approximation (not shown).

4.2 Half-quadrupole events

Figure 6 shows an example of a half-quadrupole intraseasonal event. The half-quadrupole event consists of an off-equatorial center of convective heating $\overline{H}a$, with leading off-equatorial moisture anomalies q, and a surrounding vortex structure in θ and the curl that is most pronounced in the hemisphere of heating anomalies (i.e. a half-quadrupole). In particular, this event shows strong off-equatorial v anomalies (e.g. as compared to the symmetric event from Fig. 5).

The half-quadrupole type of event may be representative of some intraseasonal convective anomalies in nature that develop off-equator over the western Pacific region (Wang and Rui, 1990; Jones et al., 2004; Izumo et al., 2010; Tung et al., 2014a, b). However, in nature those intraseasonal convective anomalies often follow convective anomalies at the equator in the Indian Ocean, that bifurcate either northward (in boreal summer) or southward (in boreal winter) when reaching the maritime continent (Wang and Rui, 1990; Jones et al., 2004). This peculiar behaviour found in nature is sometimes observed in the model solutions when a symmetric event transits to a half-quadrupole event when reaching the warm pool zonal center corresponding to the maritime continent in nature (not shown).

The half-quadrupole event shown in Fig. 6 has maximum anomalies in the northern hemisphere. For clarity, we denote this type of event as a half-quadrupole north event. There are also examples in the model solutions of half-quadrupole events with maximum anomalies in the southern hemisphere (e.g. at simulation time 74800 days in Fig. 4), that we denote as half-quadrupole south events.

4.3 Tilted events

Figure 7 shows an example of a tilted intraseasonal event. The tilted event in Fig. 7 consists of a structure of convective heating $\overline{H}a$ that is oriented north-westward, i.e. tilted, with a similarly tilted leading structure of moisture anomalies q and a tilted quadrupole structure in θ and the curl. This event shows in addition strong cross-equatorial v anomalies.

The tilted type of event shows some characteristics that are similar to the ones of the summer monsoon ISO in nature. Due to its tilted structure, the eastward propagation of this type of event (at around $5\,ms^{-1}$) produces an apparent northward propagation of convective heating (at around $1.5\,ms^{-1}$) when viewed along a fixed meridional section, similar to Lawrence and Webster (2002). This tilted band of convective heating with apparent northward propagation is one of the salient features of the summer monsoon ISO in nature (Kikuchi et al., 2011), though northward propagation can be sometimes independent of eastward propagation (Webster, 1983; Wang and Rui, 1990; Jiang et al., 2004). In addition, the tilted type of event in the model solutions shows strong cross-equatorial v anomalies and a tilted quadrupole structure that is also found in nature (e.g. Lau and Waliser, 2012, chapt 2 fig 2.10; Lawrence 1999, fig 3.7).

The tilted event shown in Fig. 7 is oriented north-westward, with maximal anomalies in the northern hemisphere. For clarity, we denote this type of event as a tilted north event. There are also examples of tilted events oriented south-westward with maximal anomalies in the southern hemisphere in the model solutions (e.g. at simulation time 73000 days in Fig. 4), that we denote as tilted south events. Note that there are also examples in the model solutions of tilted events oriented north-westward (south-westward) in the southern (northern) hemisphere, that are not considered here (not shown).

4.4 Approximate Structures of intraseasonal events

Here we provide a simplified description of the structure of the three type of intraseasonal events (symmetric, half-quadrupole and tilted events) found in the solutions of the stochastic skeleton model with seasonal cycle. The approximate structure of those events can be retrieved with good accuracy by considering the atmospheric response to prescribed heating structures $\overline{H}a$ propagating eastward at constant speed, in a fashion similar to Chao (1987) (see also Biello and Majda, 2005, 2006).

We consider prescribed heating anomalies on the equatorial and first northward zonal stochastic strips of the skeleton model (cf Fig. 1 and Eq. 12). This reads, in non-dimensional units:

$$\begin{aligned}
\overline{H}a_0 - s_0^\theta &= \overline{H}a_E \cos(kx - \omega t) \\
\overline{H}a_1 - s_1^\theta &= \overline{H}a_N \cos(kx - \omega t - b) \\
\overline{H}a_l - s_l^\theta &= 0,\ l = -2,\ -1,\ 2
\end{aligned} \tag{17}$$

where a_E, a_N, and b are prescribed parameters. For the truncation $M = 5$ adopted in the present article a_0 is the planetary enveloppe of synoptic/convective activity on the zonal stochastic strip $l = 0$ located at the equator, and a_1 is the planetary envelope of synoptic/convective activity on the zonal stochastic strip $l = 1$ located at around 1500 km north (see Fig. 1).

The above prescribed heating anomalies are considered in the skeleton model from Eq. (2), where they replace the stochastic parametrization from Eq. (3). We assume steady-state solutions taken in a moving frame with speed which is approximatively the one of the MJO, $c_F = 5\,ms^{-1}$; this is obtained by applying the variable change $\partial_t = -c_F \partial_x$ in Eq. (2). The approach is similar to the one of Chao (1987) (see also Biello and Majda, 2005, 2006); however here there is no frictional dissipation and the evolution of lower level moisture q is also considered.

Figure 8 (top) shows the prescribed heating and associated atmospheric response for a symmetric event. For this event, we consider equatorial heating anomalies only: $a_E = 0.06$ (such that $\overline{H}a \approx 0.6\,Kday^{-1}$ at the equator), $a_N = 0$ and $b = 0$. We also choose a wavenumber $k = 1$ in Fig. 8 for illustration. The atmospheric response is overall consistent with the one of the individual event from Fig. 5, and is in essence the MJO quadrupole vortex structure centered at the equator found in previous works (MS2009).

Figure 8 (middle) shows the prescribed heating and atmospheric response for a half-quadrupole north event. For this event, we consider off-equatorial convective heating only: $a_E = 0$, $a_N = 0.04$ with no phase shift so $b = 0$. The atmospheric response, located in the northern hemisphere, is overall consistent with the one of the individual event from Fig. 6, with strong off-equatorial θ, q and v anomalies. Note that a half-quadrupole south event would be retrieved by considering off-equatorial heating on the southern strip $l = -1$ instead of the northern strip $l = 1$.

Figure 8 (bottom) shows the prescribed heating and associated atmospheric response for a tilted north event. For this tilted event, we consider a combination of both equatorial and off-equatorial convective heatings, that are taken out of phase in order to produce a tilted band of convective heating oriented north-westward in the northern hemisphere: $a_E = 0.04$, $a_N = a_E$, with a phase shift $b = -\pi/2$. The atmospheric response is overall consistent with the one of the individual event from Fig. 7, with a tilted leading structure of moisture anomalies q, a tilted quadrupole structure in the curl and strong cross-equatorial v anomalies. Note that a tilted south event would be retrieved by considering off-equatorial heating on the southern strip $l = -1$ instead of the northern strip $l = 1$.

4.5 Indices of intraseasonal events

In this subsection we derive indices that estimate the amplitude of the specific types of intraseasonal events (symmetric, half-quadrupole and tilted events) found in the solutions of the stochastic skeleton model with seasonal cycle. Those indices allow one to track the occurence of each type of event through the year. The model reproduces in particular a realistic alternance of the occurence of half-quadrupole and tilted events between boreal summer/winter, as well symmetric events overall most prominent during the year.

The definition of each index is motivated from the approximate structure of individual events presented in section 4.4. Each index is computed from the component of convective heating $\overline{H}a$ over one or various zonal stochastic strips, filtered in the MJO band. For symmetric events the index is $\overline{H}a_0$, namely the $\overline{H}a$ component on the zonal stochastic strip $l = 0$ located at the equator (see Fig. 1). For half-quadrupole north events the index is $\overline{H}a_1$, while for half-quadrupole south events the index is $\overline{H}a_{-1}$. For tilted north events the index is $(\overline{H}a_0 + \overline{H}a_1^*)/2$, where a_1^* is the $\overline{H}a$ component on the northern zonal stochastic strip $l = 1$ shifted eastward by 90 degrees for each wavenumber $k = 1, 2, 3$, in a fashion similar to Eq. (17) and Fig. 8. For tilted south events the index is similarly $(\overline{H}a_0 + \overline{H}a_{-1}^*)/2$.

Figure 9 shows the longitude-time hovmoller diagrams of each index compared to a $y - t$ Hovmoller diagram of $\overline{H}a$ (identical to the one in Fig. 4e). This representation allows to track the occurence of each type of event in the simulations. As shown in Fig. 9, symmetric events are overall most prominent. The strong tilted events at simulation time 73000 days and 73800 days in particular are well captured by the associated indices, though a drawback of the present method is that they are also counted as symmetric and half-quadrupole events.

The above indices also allow to diagnose the occurence of each type of intraseasonal event through the year. Figure 3(f) shows the occurence of each type of event, as a function of seasons. The occurence of each type of event is computed based on a threshold criteria: we compute for each index a threshold criteria that is equal to unity when the index magnitude from Fig. 9 is superior to a threshold value set here at $0.2\,Kday^{-1}$, and zero otherwise. The threshold criteria is then averaged over the warm pool region ($x = 10,000$ to $30,000\,km$) and over each day of the year, which is shown in Fig. 3(f).

The occurence of each type of intraseasonal event shown in Fig. 3(f) is qualitatively consistent with the one found in nature. In particular, half-quadrupole north and tilted north events are most prominent in boreal summer as compared to boreal winter, while half-quadrupole south and tilted south events are most prominent in boreal winter as compared to boreal summer (Wang and Rui, 1990; Jones et al., 2004). Meanwhile, the symmetric events are most prominent through the entire year as compared to the other types of events. This is consistent with observations where MJO events are most prominent through the year, except during boreal summer where summer monsoon ISO (i.e. tilted north) events should be most prominent (Lawrence and Webster, 2002; Kikuchi et al., 2011).

5 Conclusions

We have analyzed the dynamics of a stochastic skeleton model for the MJO and the intraseasonal-planetary variability in general with a seasonal cycle. It is a modified version of a minimal dynamical model, the skeleton model (Majda and Stechmann, 2009b, 2011; Thual et al., 2014). The skeleton model has been shown in previous work to capture together the MJO's salient features of (I) a slow eastward phase speed of roughly $5\,ms^{-1}$, (II) a peculiar dispersion relation with $d\omega/dk \approx 0$, and (III) a horizontal quadrupole structure. Its stochastic version further includes a simple stochastic parametrization of the unresolved synoptic-scale convective/wave processes. Most notably, the stochastic skeleton model has been shown to reproduce qualitatively (IV) the intermittent generation of MJO events and (V) the organization of MJO events into wave trains with growth and demise, as in nature. In the present article, we further focus on the tropical intraseasonal variability in general simulated by the stochastic skeleton model. Two main features of the intraseasonal variability that are qualitatively reproduced by the model are:

VI. Meridionally asymmetric intraseasonal events, and

VII. A seasonal modulation of intraseasonal variability.

In order to account for features (VI-VII), two important modifications have been considered in the stochastic skeleton model with seasonal cycle. First, while in previous works with the skeleton model focusing on the MJO (Majda and Stechmann, 2009b, 2011; Thual et al., 2014) a single equatorial component of convective heating was considered, here we have considered additional off-equatorial components of convective heating in order to further produce meridionally asymmetric intraseasonal events beyond the MJO. Second, a simple seasonal cycle has been included that consists in a background warm pool state of heating/moistening that migrates meridionally during the year.

A new feature of the stochastic skeleton model with seasonal cycle, as compared to previous works with the skeleton model, is the simulation of a large diversity of meridionally symmetric and asymmetric intraseasonal-planetary events. Indeed, in nature intraseasonal events show a great diversity in horizontal structure, strength, lifetime and localization (Wang and Rui, 1990; Jones et al., 2004; Masunaga, 2007). For example, both equatorial and off-equatorial convective heating coexist during intraseasonal events with characteristics and intensity that differ from one event to another, including during MJO events (Tung et al., 2014a, b; Biello and Majda, 2005, 2006). The present stochastic skeleton model with seasonal cycle qualitatively reproduces this diversity of intraseasonal events. In addition, despite their diversity those intraseasonal events are organized into intermittent wave trains with growth and demise, i.e. into series of successive events following a primary intraseasonal event, as seen in nature (Matthews, 2008; Yoneyama et al., 2013; Thual et al., 2014). This is an attractive feature of the stochastic skeleton model with seasonal cycle in generating intraseasonal variability.

While the stochastic skeleton model with seasonal cycle obviously lacks several key physical processes in order to account for the complete dynamics of the MJO and intraseasonal variability in general, e.g. topographic effects, land-sea contrast, a refined vertical structure, mean vertical shears, etc (Lau and Waliser, 2012 chapt 10, 11), it is interesting that some aspects of peculiar intraseasonal events found in nature are qualitatively recovered in the model solutions. Three interesting types of intraseasonal-planetary events found in the model solutions are symmetric events, half-quadrupole events, and tilted events. As regards observations, the symmetric events with quadrupole vortex structure are most representative of MJO composites (Hendon and Salby, 1994; Majda and Stechmann, 2009b). The half-quadrupole events, with off-equatorial heating structure may be representative of some intraseasonal convective anomalies that develop off-equator in the western Pacific, though in nature those convective anomalies often follow convective anomalies at the equator in the Indian Ocean (Wang and Rui, 1990; Jones et al., 2004; Izumo et al., 2010; Tung et al., 2014a, b). Finally, the tilted events with a heating structure oriented north-westward and strong cross-equatorial flow share some characteristics with the summer monsoon intraseasonal oscillation: in particular, the eastward propagation of those events (at around $5\,ms^{-1}$) results in apparent northward propagations (at around $1.5\,ms^{-1}$) when viewed along a latitudinal section, similar to Lawrence and Webster (2002). While the three above types of events have an appealing theoretical basis and corresponding observational surrogates, we note that there are other types of intraseasonal events simulated by the stochastic skeleton model with seasonal cycle that have not been analyzed in detail here, and that may be of importance. This diversity of intraseasonal events could be further analyzed in future work. For example some events simulated by the present model may be characterized as being of a mixed type, e.g. as resulting from a combination of the three above types of events, or as transiting from one event type to another during their lifetime. This includes examples of intraseasonal events transiting from a symmetric event to a half-quadrupole event when reaching the warm pool center corresponding to the maritime continent in nature (Wang and Rui, 1990; Jones et al., 2004).

The intraseasonal-planetary variability in nature migrates meridionally during the year, approximatively following the migration of warm sea surface temperatures (Salby and Hendon, 1994; Zhang and Dong, 2004). This feature is qualitatively recovered by the stochastic skeleton model with seasonal cycle, despite the fact that the present model considers a qualitative truncation of the planetary-scale circulation to a few main components. For example, the meridional displacement is different for each variable, which is related to the meridional shape of the few equatorial Kelvin and Rossby waves considered here (cf section 2). Nevertheless the model exhibits a strong off-equatorial intraseasonal variability in both boreal summer and winter, with potential implications for understanding its interactions with the Asian and Australian monsoon (Wheeler and Hendon, 2004; Lau and Waliser, 2012 chapt 2, 5). In addition, we have verified that the occurence of the three above types of intraseasonal events during the year is qualititatively consistent with observations. For instance, tilted events with heating structure oriented north-westward and half-quadrupole events with northern off-equatorial heating structure are more prominent in boreal summer as compared to the other seasons (Wang and Rui, 1990; Jones et al., 2004). Meanwhile, symmetric events are the most prominent type of event through the entire year, consistent with observations where MJO events are most prominent through the year except during boreal summer where summer monsoon ISO (i.e. tilted north) events should be most prominent (Lawrence and Webster, 2002; Kikuchi et al., 2011).

While the skeleton model appears to be a plausible representation for the essential mechanisms of the MJO and some aspects of intraseasonal variability in general, several issues need to be adressed as a perspective for future work. One important issue is to compare further the skeleton model solutions with their observational surrogates, qualitatively and also quantitatively. A more complete model should also account for more detailed sub-planetary processes within the envelope of intraseasonal events, including for example synoptic-scale convectively coupled waves and/or mesoscale convective systems (e.g. Moncrieff et al., 2007; Majda et al., 2007; Khouider et al., 2010; Frenkel et al., 2012).

Acknowledgements: The research of A.J.M. is partially supported by the Office of Naval Research Grant ONR MURI N00014 -12-1-0912. The research of S.N.S. is partially supported by the Office of Naval Research Grants ONR YIP N00014-12-1-0744 and ONR MURI N00014-12-1-0912. S.T. is supported as a postdoctoral fellow through A.J.M's ONR MURI Grant.

References

Ajayamohan, R. S., Khouider, B., and Majda, A. J. (2013). Realistic initiation and dynamics of the Madden-Julian Oscillation in a coarse resolution aquaplanet GCM. *Geophys. Res. Lett.*, 40:6252–6257.

Annamalai, H. and Sperber, K. R. (2005). Regional Heat Sources and the Active and Break Phases of Boreal Summer Intraseasonal (30-50 Day) Variability. *J. Atmos. Sci.*, 62:2726–2748.

Biello, J. A. and Majda, A. J. (2005). A new multiscale model for the madden-julian oscillation. *J. Atmos. Sci.*, 62(6):1694–1721.

Biello, J. A. and Majda, A. J. (2006). Modulating synoptic scale convective activity and boundary layer dissipation in the IPESD models of the Madden-Julian oscillation. *Dyn. Atm. Oceans*, 42(1-4):152–215.

Chao, W. C. (1987). On the origin of the tropical intraseasonal oscillation. *J. Atmos. Sci.*, 44(15):1940–1949.

Deng, Q., Khouider, B., and Majda, A. J. (2014). The MJO in a Coarse-Resolution GCM with a Stochastic Multicloud Parameterization. *J. Atmos. Sci.* submitted.

Dias, J., Leroux, S., Tulich, S. N., and Kiladis, G. N. (2013). How systematic is organized tropical convection within the MJO? *Geophys. Res. Lett.*, 40:1420–1425.

Frenkel, Y., Majda, A. J., and Khouider, B. (2012). Using the stochastic multicloud model to improve tropical convective parameterization: A paradigm example. *J. Atmos. Sci.*, 69(3):1080–1105.

Gardiner, C. W. (1994). *Handbook of stochastic methods for physics, chemistry, and the natural sciences*. Springer.

Gill, A. (1980). Some simple solutions for heat-induced tropical circulation. *Quart. J. Roy. Meteor. Soc.*, 106:447–462.

Goswami, B. N., Ajayamohan, R. S., Xavier, P. K., and Sengupta, D. (2003). Clustering of synoptic activity by Indian symmer monsoon intraseasonal oscillations. *Geophys. Res. Lett.*, 8:1–14. doi:10.1029/2002GL016734.

Grabowski, W. W. and Moncrieff, M. W. (2004). Moisture-convection feedback in the Tropics. *Quart. J. Roy. Meteor. Soc.*, 130:3081–3104.

Hendon, H. H. and Liebmann, B. (1994). Organization of convection within the Madden-Julian oscillation. *J. Geophys. Res.*, 99:8073–8083.

Hendon, H. H. and Salby, M. L. (1994). The life cycle of the madden-julian oscillation. *J. Atmos. Sci.*, 51(15):2225–2237.

Holloway, C. E. and Neelin, J. D. (2009). Moisture Vertical Structure, Column Water Vapor, and Tropical Deep Convection. *J. Atmos. Sci.*, 66:1665–1683.

Hung, M.-P., Lin, J.-L., Wang, W., Kim, D., Shinoda, T., and Weaver, S. J. (2013). Mjo and convectively coupled equatorial waves simulated by cmip5 climate models. *J. Climate*, 26:6185–6214.

Izumo, T., Masson, S., Vialard, J., de Boyer Montegut, C., Behera, S. K., Madec, G., Takahashi, K., and Yamagata, T. (2010). Low and high frequency Madden-Julian oscillations in austral summer: interannual variations. *Clim. Dyn.*, 35:669–683.

Jiang, X., Li, T., and Wang, B. (2004). Structures and mechanisms of the northward propagating boreal summer intraseasonal oscillation. *J. Climate*, 17:1022–1039.

Jones, C., Carvalho, L. M., Higgins, R. W., Waliser, D. E., and Schemm, J.-K. E. (2004). Climatology of Tropical Intraseasonal Convective Anomalies: 1979-2002. *J. Climate*, 17:523–539.

Khouider, B., Biello, J. A., and Majda, A. J. (2010). A stochastic multicloud model for tropical convection. *Comm. Math. Sci.*, 8(1):187–216.

Khouider, B. and Majda, A. J. (2006). A simple multicloud parametrization for convectively coupled tropical waves. Part I: Linear Analysis. *J. Atmos. Sci.*, 63:1308–1323.

Khouider, B., St-Cyr, A., Majda, A. J., and Tribbia, J. (2011). The MJO and convectively coupled waves in a coarse-resolution GCM with a simple multicloud parameterization. *J. Atmos. Sci.*, 68(2):240–264.

Kikuchi, K. and Takayabu, Y. N. (2004). The development of organized convection associated with the MJO during TOGA COARE IOP: Trimodal characteristics. *Geophys. Res. Lett.*, 31. L10101,doi:10.1029/2004GL019601.

Kikuchi, K., Wang, B., and Kajikawa, Y. (2011). Bimodal representation of the tropical intraseasonal oscillation. *Clim. Dyn.* DOI 10.1007/s00382-011-1159-1.

Kiladis, G. N., Straub, K. H., and T., H. P. (2005). Zonal and vertical structure of the Madden-Julian oscillation. *J Atmos Sci*, 62:2790–2809.

Kiladis, G. N., Wheeler, C., Haertel, P. T., Straub, K. H., and Roundy, P. E. (2009). Convectively coupled equatorial waves. *Rev. Geophys.*, 47. RG2003, doi:10.1029/2008RG000266.

Kim, D., K., S., Stern, W., Waliser, D., Kang, I.-S., Maloney, E., Wang, W., Weickmann, K., Benedict, J., Khairoutdinov, M., Lee, M.-I., Neale, R., Suarez, M., Thayer-Calder, K., and Zhang, G. (2009). Application of MJO simulation diagnostics to climate models. *J. Climate*, 22:6413–6436.

Lau, K.-M. and Peng, L. (1990). Origin of Low Frequency (Intraseasonal) Oscillations in the Tropical Atmosphere. Part III: Monsoon Dynamics. *J. Atmos. Sci.*, 47:1443–1462.

Lau, W. M. and Waliser, D. E. (2012). *Intraseasonal Variability in the Atmosphere-Ocean Climate System.* Springer. 642pp.

Lawler, G. F. (2006). *Introduction to Stochastic Processes.* CRC Press.

Lawrence, D. M. and Webster, P. J. (2002). The boreal summer intraseasonal oscillation: Relationship between northward and eastward movement of convection. *J. Atmo. Sci.*, 59:1593–1606.

Lawrence, M. (1999). Intraseasonal Variability of the South Asian Monsoon. *PhD thesis.* 195pp.

Lin, J.-L., Kiladis, G. N., Mapes, B. E., Weickmann, K. M., Sperber, K. R., Lin, W., Wheeler, M. C., Schubert, S. D., Del Genio, A., Donner, L. J., Emori, S., Gueremy, J.-F., Hourdin, F., Rasch, P. J., Roeckner, E., and Scinocca, J. F. (2006). Tropical intraseasonal variability in 14 IPCC AR4 climate models. part i: Convective signals. *J. Climate*, 19(12):2665–2690.

Madden, R. E. and Julian, P. R. (1971). Detection of a 40-50 day oscillation in the zonal wind in the tropical Pacific. *J. Atmos. Sci.*, 28:702–708.

Madden, R. E. and Julian, P. R. (1994). Observations of the 40-50 day tropical oscillation-A review. *Mon. Wea. Rev.*, 122:814–837.

Majda, A. J. and Biello, J. A. (2004). A multiscale model for tropical intraseasonal oscillations. *Proc. Natl. Acad. Sci. USA*, 101(14):4736–4741.

Majda, A. J., Franzke, C., and Khouider, B. (2008). An applied mathematics perspective on stochastic modelling for climate. *Philos. Trans.Roy. Soc.*, A366(1875):2427–2453.

Majda, A. J. and Khouider, B. (2001). A numerical strategy for efficient modeling of the equatorial wave guide. *Proc. Natl. Acad. Sci. USA*, 98(4):1341–1346.

Majda, A. J. and Klein, R. (2003). Systematic Multi-Scale Models for the Tropics. *J. Atmos. Sci.*, 60:357–372.

Majda, A. J. and Stechmann, S. N. (2009a). A simple dynamical model with features of convective momentum transport. *J. Atmos. Sci.*, 66(2):373–392.

Majda, A. J. and Stechmann, S. N. (2009b). The skeleton of tropical intraseasonal oscillations. *Proc. Natl. Acad. Sci. USA*, 106(21):8417–8422.

Majda, A. J. and Stechmann, S. N. (2011). Nonlinear dynamics and regional variations in the MJO skeleton. *J. Atmos. Sci.*, 68(12):3053–3071.

Majda, A. J., Stechmann, S. N., and Khouider, B. (2007). Madden-Julian oscillation analog and intraseasonal variability in a multicloud model above the equator. *Proc. Natl. Acad. Sci. USA*, 104:9919–9924.

Masunaga, H. (2007). Seasonality and Regionality of the Madden-Julian Oscillation, Kelvin Wave, and Equatorial Rossby Wave. *J. Atmos. Sci.*, 64:4400–4416.

Matthews, A. J. (2008). Primary and successive events in the Madden-Julian Oscillation. *Quart. J. Roy. Meteor. Soc.*, 134:439–453.

Moncrieff, M. (2004). Analytic representation of the large-scale organization of tropical convection. *Quart. J. Roy. Meteor. Soc.*, 130:1521–1538.

Moncrieff, M. W., Shapiro, M., Slingo, J., and Molteni, F. (2007). Collaborative research at the intersection of weather and climate. *WMO Bull.*, 56:204–211.

Salby, M. L. and Hendon, H. H. (1994). Intraseasonal behavior of clouds, temperature, and winds in the tropics. *J. Atmos. Sci.*, (51):2207–2224.

Sobel, A. H., Nilsson, J., and Polvani, L. M. (2001). The Weak Temperature Gradient Approximation and Balanced Tropical Moisture Waves. *J. Atmos. Sci.*, 58:3650–3665.

Stechmann, S., Majda, A. J., and Skjorshammer, D. (2013). Convectively coupled wave-environment interactions. *Theor. Comput. Fluid Dyn.*, 27:513–532.

Stechmann, S. N. and Neelin, J. D. (2011). A stochastic model for the transition to strong convection. *J. Atmos. Sci.*, 68(12):2955–2970.

Straub, K. H. and Kiladis, G. N. (2003). Interactions between the Boreal Summer Intraseasonal Oscillation and Higher-Frequency Tropical Wave Activity. *Mon. Wea. Rev.*, 131:945–960.

Thual, S., Majda, A. J., and Stechmann, S. N. (2014). A stochastic skeleton model for the MJO. *J. Atmos. Sci.*, 71:697–715.

Tian, B., Waliser, D., Fetzer, E., Lambrigsten, B., Yung, Y., and Wang, B. (2006). Vertical moist thermodynamic structure and spatial-temporal evolution of the MJO in AIRS observations. *J. Atmos. Sci.*, 63:2462–2485.

Tung, W.-W., Giannakis, D., and Majda, A. J. (2014a). Symmetric and antisymmetric convection signals in the Madden-Julian oscillation. Part I: Basic modes in infrared brightness temperature. *J.Atmos.Sci., submitted.*

Tung, W.-W., Giannakis, D., and Majda, A. J. (2014b). Symmetric and antisymmetric convection signals in the Madden-Julian oscillation. Part II: Kinematics and thermodynamics. *J.Atmos.Sci., submitted.*

Wang, B. and Rui, H. (1990). Synoptic Climatology of Transient Tropical Intraseasonal Convection Anomalies: 1975-1985. *Meteorol.Atmos.Phys.*, 44:43–61.

Wang, B. and Xie, X. (1997). A model for the boreal summer intraseasonal oscillation. *J.Atmos.Sci*, 54:72–86.

Webster, P. J. (1983). Mechanisms of Monsoon Low-Frequency Variability: Surface Hydrological Effects. *J. Atmos. Sci.*, 40:2110–2124.

Wheeler, M. and Kiladis, G. N. (1999). Convectively coupled equatorial waves: Analysis of clouds and temperature in the wavenumber-frequency domain. *J. Atmos. Sci.*, 56(3):374–399.

Wheeler, M. C. and Hendon, H. H. (2004). An all-season real-time multivariate mjo index: Development of an index for monitoring and prediction. *Mon. Wea. Rev.*, 132:1917–1932.

Yoneyama, K., Zhang, C., and Long, C. N. (2013). Tracking Pulses of the Madden-Julian Oscillation. *Bull. Am. Meteor. Soc.*, 94:1871–1891.

Zhang, C. (2005). Madden-julian oscillation. *Rev. Geophys.*, 43. RG2003, doi:10.1029/2004RG000158.

Zhang, C. and Dong, M. (2004). Seasonality in the madden-julian oscillation. *J. Climate.*, 17:3169–3180.

Figure Captions:

Figure 1: Model spectral and physical space and warm pool shape: Hermite functions ϕ_m, $m = 0, 1, 2$ (lines) and zonal strips positions y_l, $-(M-1)/2 \leq l \leq (M-1)/2$ (dots) for a truncation $M = 5$, as a function of y in 1000km.

Figure 2: Zonal wavenumber-frequency power spectra: for (a) u (ms^{-1}), (b) θ (K), (c) q (K), and (d)$\overline{H}a$ $(Kday^{-1})$, as a function of zonal wavenumber (in $2\pi/40000km$) and frequency (in cpd). The contour levels are in the base 10-logarithm, for the dimensional variables averaged within 1500 km south/north. The black dashed lines mark the periods 90 and 30 days.

Figure 3: Intraseasonal activity: for (a) u $(m.s^{-1})$, (b) v (ms^{-1}), (c) θ (K), (d) q (K), and (e) $\overline{H}a$ $(K.day^{-1})$, as a function of season (month of the year) and meridional position y (1000 km). The intraseasonal activity is computed as the standard deviation of signals filtered in the MJO band ($1 \leq k \leq 3$ and $1/90 \leq \omega \leq 1/30$ cpd) averaged over the warm pool region ($x = 10,000$ to $30,000\,km$). (f): Occurence of each type of intraseasonal event: for half-quadrupole south (blue), tilted south (green), symmetric (black), tilted north (magenta), and half-quadrupole north (red) events, nondimensional and as a function of season (month of the year, x-axis).

Figure 4: $y-t$ Hovmoller diagrams: for (a) u $(m.s^{-1})$, (b) v $(m.s^{-1})$, (c) θ (K), (d) q (K), and (e) $\overline{H}a$ $(K.day^{-1})$, as a function of meridional position location y (in 1000 km) and simulation time (in 1000 days). (f) repeats the Hovmoller diagram for $\overline{H}a$ at different times. The variables are filtered in the MJO band ($1 \leq k \leq 3$ and $1/90 \leq \omega \leq 1/30$ cpd), and considered at the warm pool zonal center ($x = 20,000\,km$). The meridional position y_C of the warm pool center, varying with seasons, is overplotted (black line).

Figure 5: $x-y$ Snapshots for a symmetric intraseasonal event: for (a) u (ms^{-1}), (b) v (ms^{-1}), (c) θ (K), (d) q (K), (e) $\overline{H}a$ $(Kday^{-1})$, (f) divergence $\partial_x u + \partial_y v$ $(m.s^{-1})(1000km)^{-1}$, and (g) curl $\partial_x v - \partial_y u$ $(m.s^{-1})(1000km)^{-1}$, as a function of zonal position x (1000km) and meridional position y (1000km). Left label indicates simulation time for each snapshot (in days). The variables are filtered in the MJO band ($1 \leq k \leq 3$ and $1/90 \leq \omega \leq 1/30$ cpd). Tick marks indicate the equator.

Figure 6: Same as Fig. 5, but for the case of a half-quadrupole north event.

Figure 7: Same as Fig. 5, but for the case of a tilted north event.

Figure 8: Atmospheric response to prescribed heating: for (a) u (ms^{-1}), (b) v (ms^{-1}), (c) θ (K), (d) q (K), (e) $\overline{H}a$ ($Kday^{-1}$), (f) divergence $\partial_x u + \partial_y v$ $(m.s^{-1})(1000km)^{-1}$, and (g) curl $\partial_x v - \partial_y u$ $(m.s^{-1})(1000km)^{-1}$, as a function of zonal position x (1000km) and meridional position y (1000km). This is shown for (top) a symmetric event, (middle) a half-quadrupole north event, (bottom) a tilted north event.

Figure 9: (a) $y-t$ Hovmoller diagram: for $\overline{H}a$ ($Kday^{-1}$), as a function of meridional position location y (in 1000 km) and simulation time (in 1000 days), considered at the warm pool zonal center ($x = 20,000\,km$). (b-f): $x-t$ Hovmoller diagrams: for the index of (b) half-quadrupole south (HQS), (c) tilted south (TS), (d) symmetric (SY), (e) tilted north (TN), and (f) half-quadrupole north (HQN) events, in $Kday^{-1}$ and as a function of zonal position location x (in 1000 km) and simulation time (1000 days).

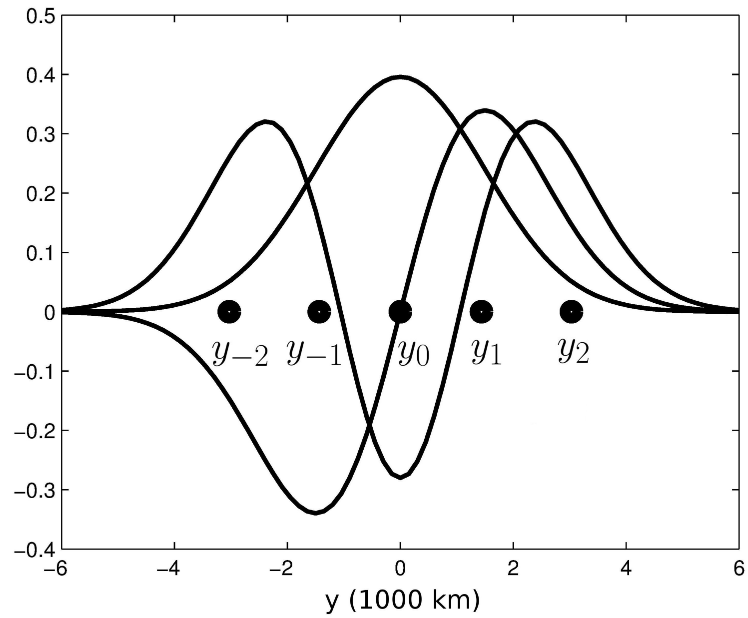

Figure 1: Model spectral and physical space and warm pool shape: Hermite functions ϕ_m, $m = 0, 1, 2$ (lines) and zonal strips positions y_l, $-(M-1)/2 \leq l \leq (M-1)/2$ (dots) for a truncation $M = 5$, as a function of y in 1000km.

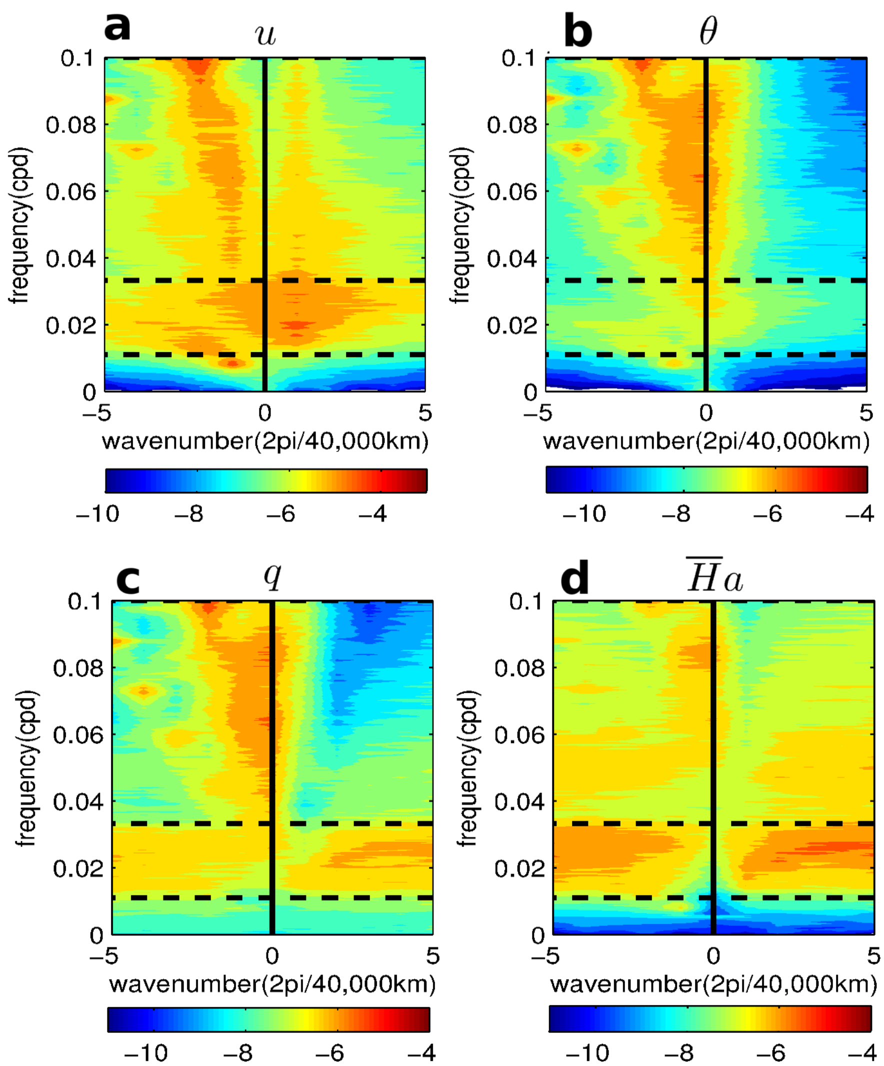

Figure 2: Zonal wavenumber-frequency power spectra: for (a) u (ms^{-1}), (b) θ (K), (c) q (K), and (d)$\overline{H}a$ ($Kday^{-1}$), as a function of zonal wavenumber (in $2\pi/40000km$) and frequency (in cpd). The contour levels are in the base 10-logarithm, for the dimensional variables averaged within $1500\,km$ south/north. The black dashed lines mark the periods 90 and 30 days.

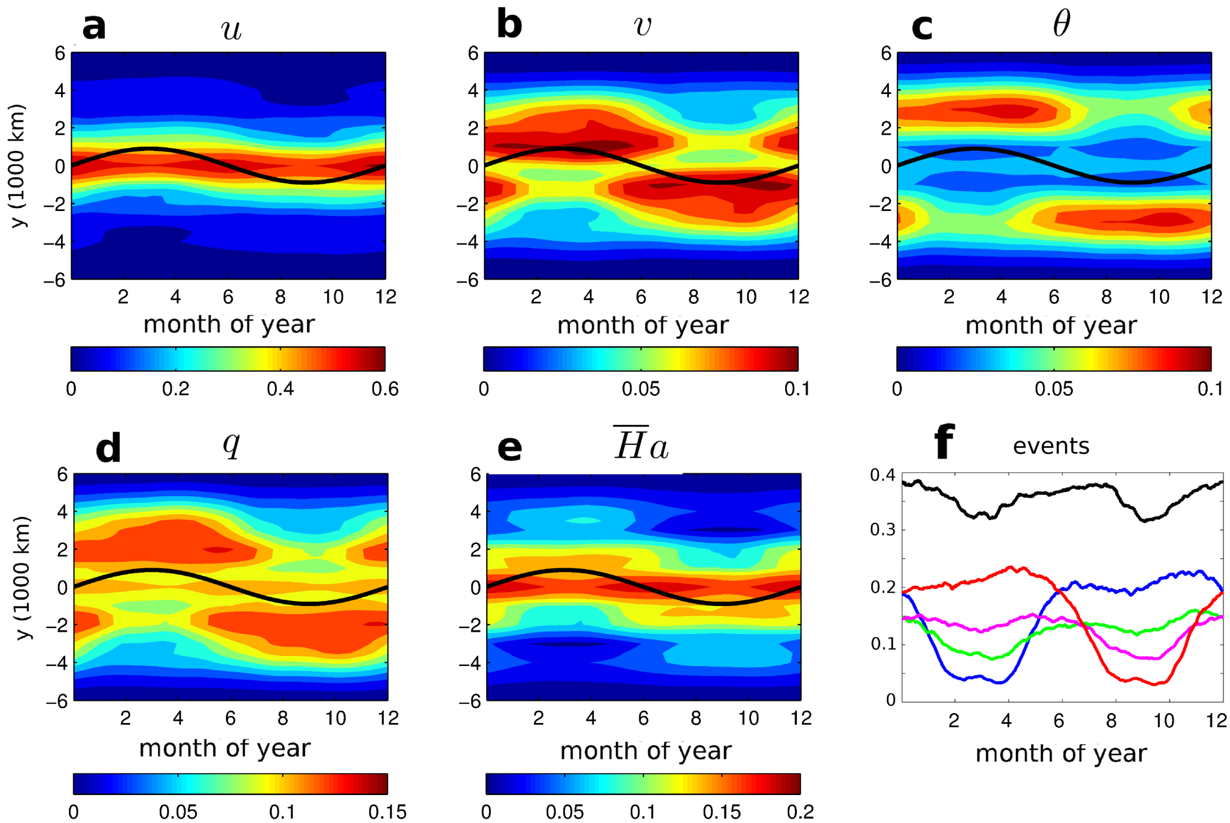

Figure 3: Intraseasonal activity: for (a) u ($m.s^{-1}$), (b) v (ms^{-1}), (c) θ (K), (d) q (K), and (e) $\overline{H}a$ ($K.day^{-1}$), as a function of season (month of the year) and meridional position y (1000 km). The intraseasonal activity is computed as the standard deviation of signals filtered in the MJO band ($1 \leq k \leq 3$ and $1/90 \leq \omega \leq 1/30$ cpd) averaged over the warm pool region ($x = 10,000$ to $30,000\,km$). (f): Occurence of each type of intraseasonal event: for half-quadrupole south (blue), tilted south (green), symmetric (black), tilted north (magenta), and half-quadrupole north (red) events, nondimensional and as a function of season (month of the year, x-axis).

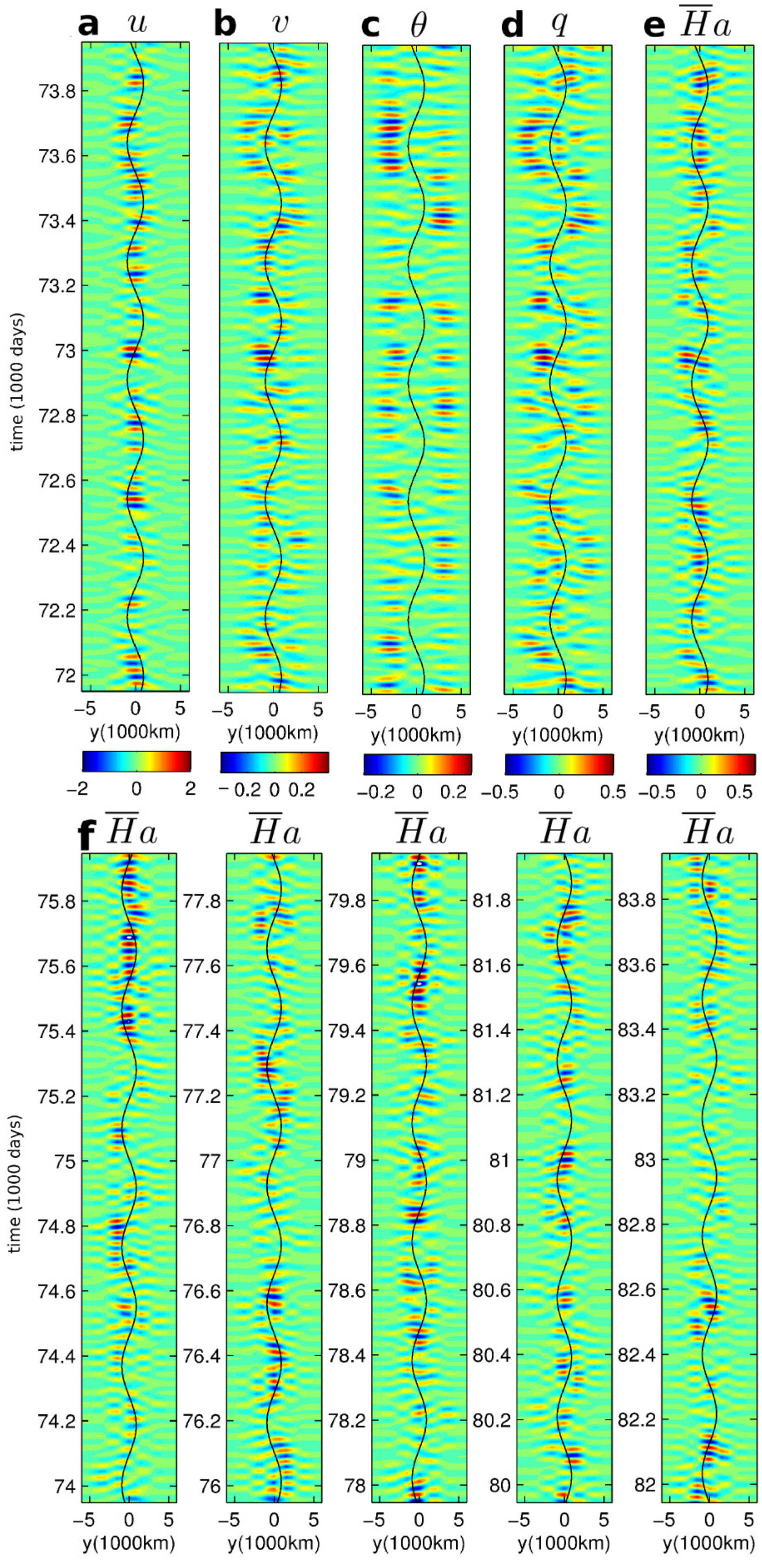

Figure 4: $y-t$ Hovmoller diagrams: for (a) u ($m.s^{-1}$), (b) v ($m.s^{-1}$), (c) θ (K), (d) q (K), and (e) $\overline{H}a$ ($K.day^{-1}$), as a function of meridional position location y (in 1000 km) and simulation time (in 1000 days). (f) repeats the Hovmoller diagram for $\overline{H}a$ at different times. The variables are filtered in the MJO band ($1 \leq k \leq 3$ and $1/90 \leq \omega \leq 1/30$ cpd), and considered at the warm pool zonal center ($x = 20,000\,km$). The meridional position y_C of the warm pool center, varying with seasons, is overplotted (black line).

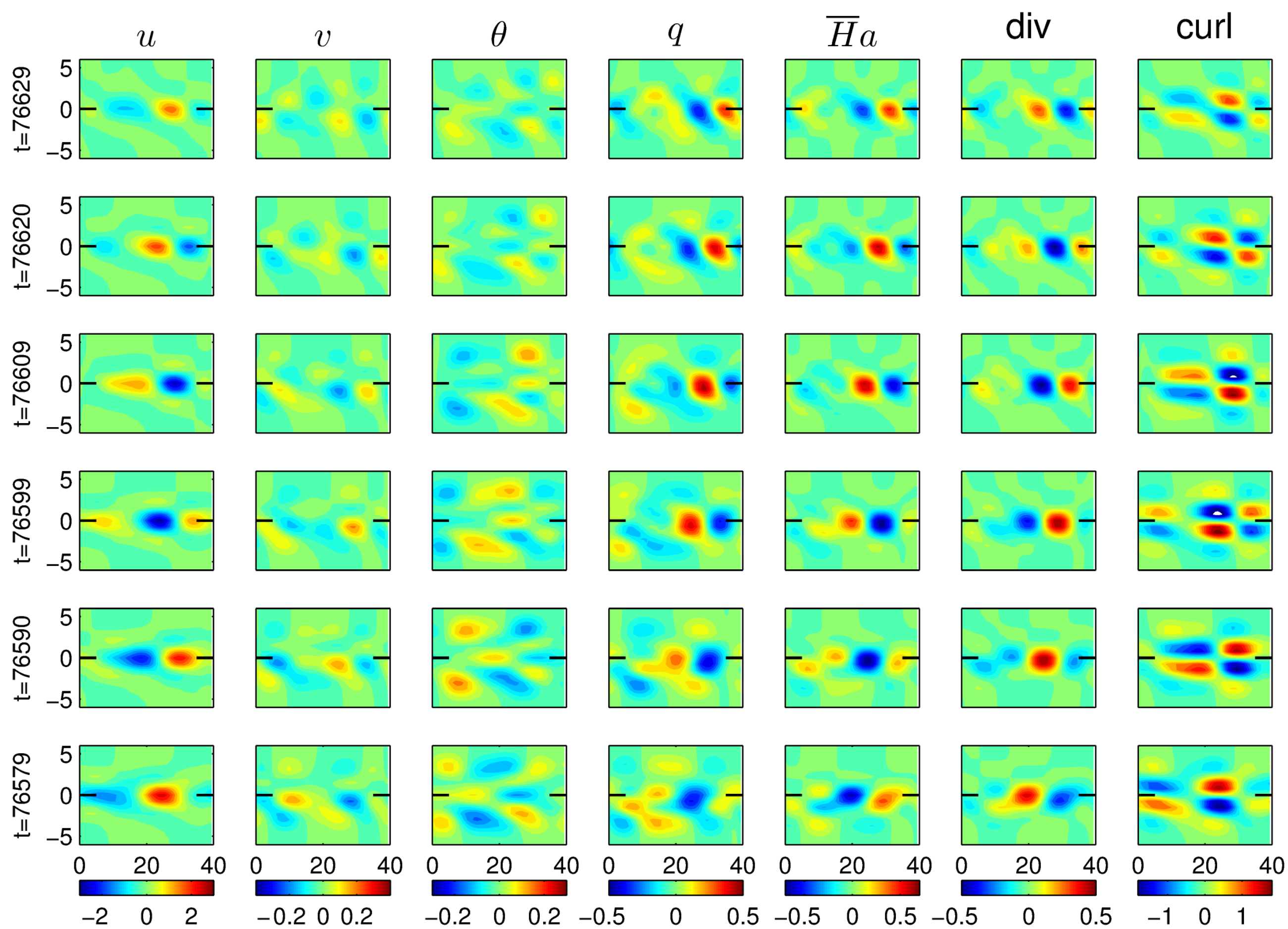

Figure 5: $x-y$ Snapshots for a symmetric intraseasonal event: for (a) u (ms^{-1}), (b) v (ms^{-1}), (c) θ (K), (d) q (K), (e) $\overline{H}a$ ($Kday^{-1}$), (f) divergence $\partial_x u + \partial_y v$ ($m.s^{-1}$)($1000km$)$^{-1}$, and (g) curl $\partial_x v - \partial_y u$ ($m.s^{-1}$)($1000km$)$^{-1}$, as a function of zonal position x (1000km) and meridional position y (1000km). Left label indicates simulation time for each snapshot (in days). The variables are filtered in the MJO band ($1 \leq k \leq 3$ and $1/90 \leq \omega \leq 1/30$ cpd). Tick marks indicate the equator.

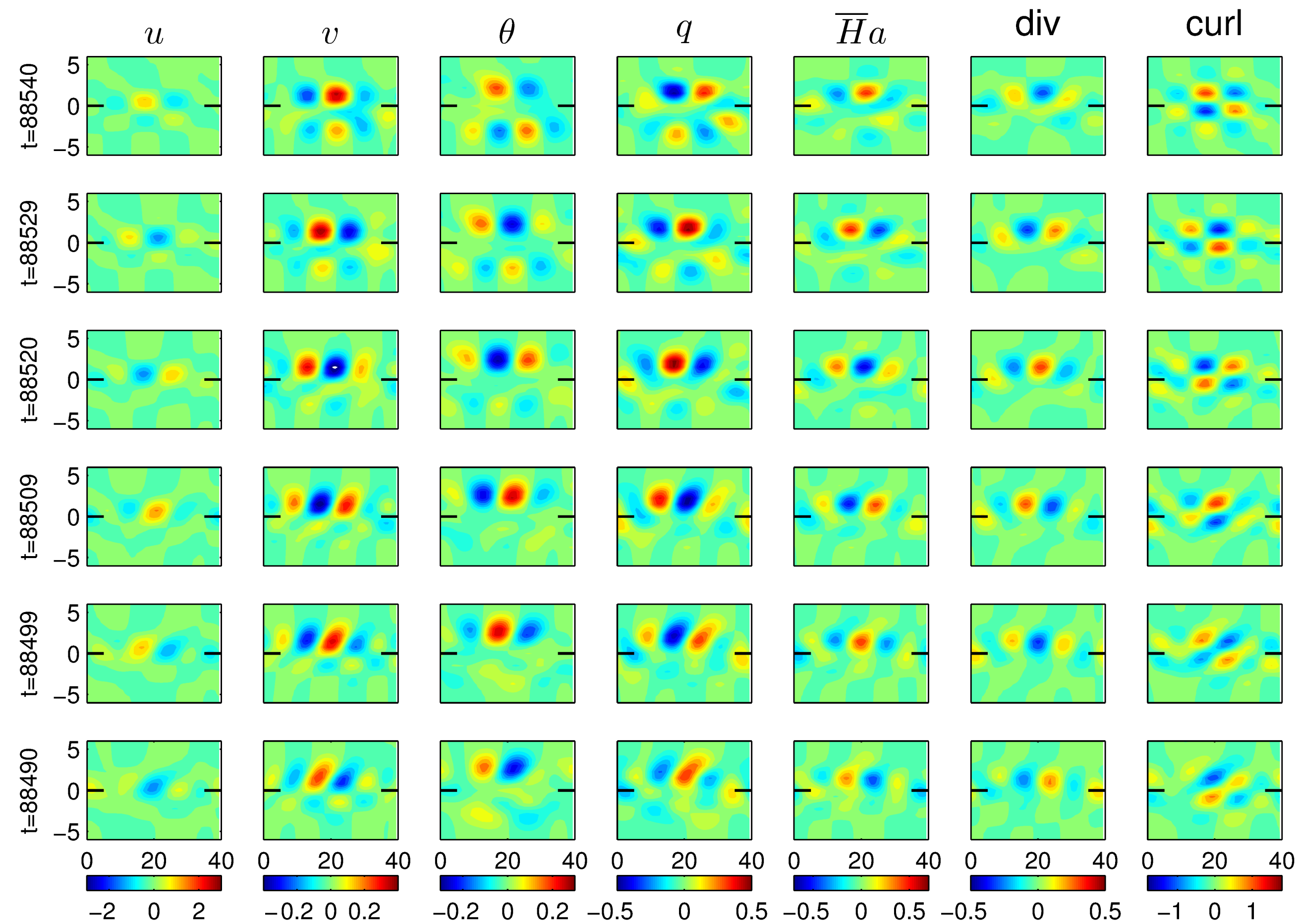

Figure 6: Same as Fig. 5, but for the case of a half-quadrupole north event.

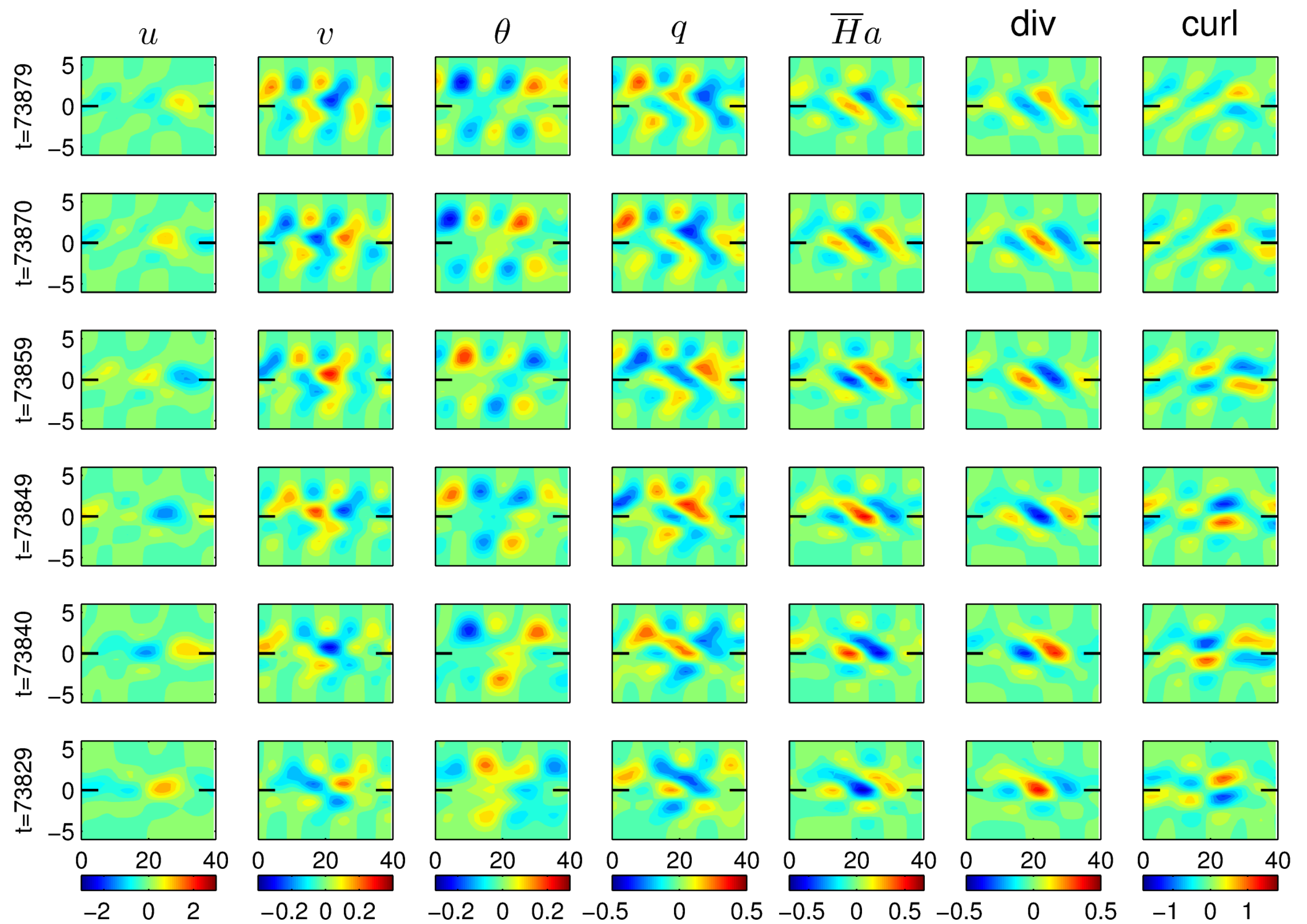

Figure 7: Same as Fig. 5, but for the case of a tilted north event.

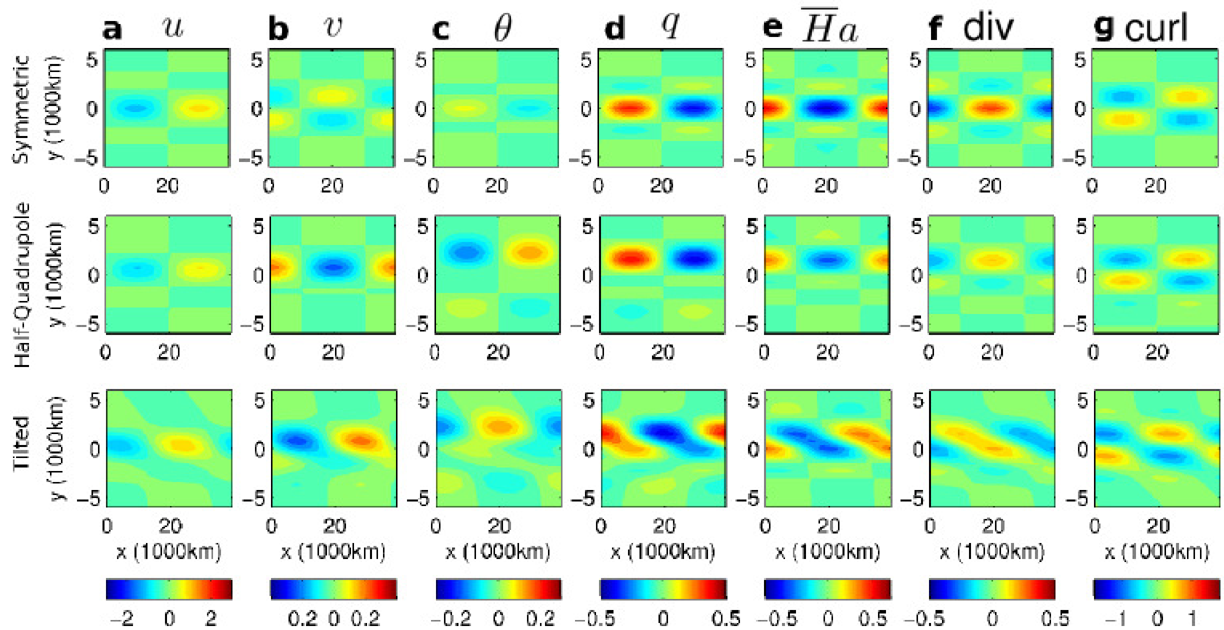

Figure 8: Atmospheric response to prescribed heating: for (a) u (ms^{-1}), (b) v (ms^{-1}), (c) θ (K), (d) q (K), (e) $\overline{H}a$ ($Kday^{-1}$), (f) divergence $\partial_x u + \partial_y v$ ($m.s^{-1}$)($1000km$)$^{-1}$, and (g) curl $\partial_x v - \partial_y u$ ($m.s^{-1}$)($1000km$)$^{-1}$, as a function of zonal position x (1000km) and meridional position y (1000km). This is shown for (top) a symmetric event, (middle) a half-quadrupole north event, (bottom) a tilted north event. .

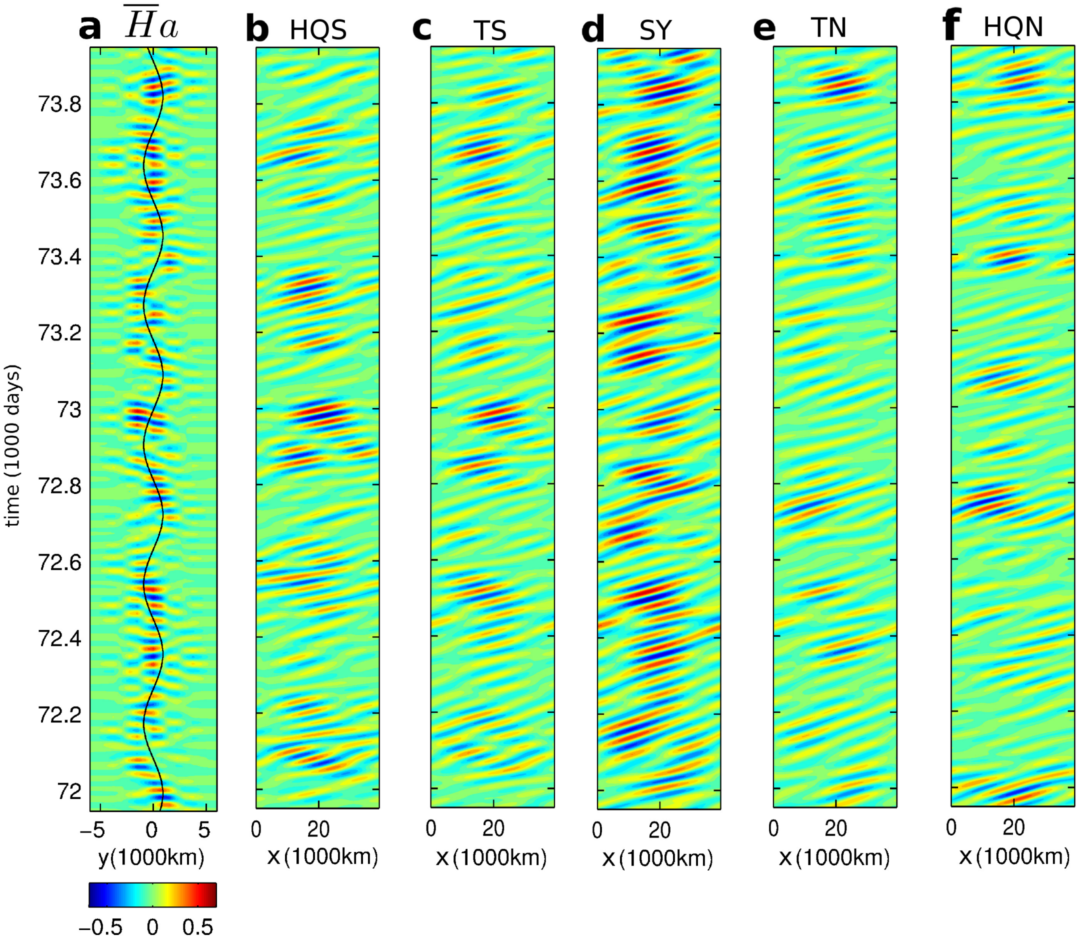

Figure 9: (a) $y-t$ Hovmoller diagram: for $\overline{H}a$ ($Kday^{-1}$), as a function of meridional position location y (in 1000 km) and simulation time (in 1000 days), considered at the warm pool zonal center ($x = 20,000\,km$). (b-f): $x-t$ Hovmoller diagrams: for the index of (b) half-quadrupole south (HQS), (c) tilted south (TS), (d) symmetric (SY), (e) tilted north (TN), and (f) half-quadrupole north (HQN) events, in $Kday^{-1}$ and as a function of zonal position location x (in 1000 km) and simulation time (1000 days).